

# Evaluation of Deep Learning-based Scatter Correction for Total-body PET

Baptiste Laurent<sup>1</sup>, Alexandre Bousse<sup>1\*</sup>, Thibaut Merlin<sup>1</sup>, Axel Rominger<sup>2</sup>,  
Kuangyu Shi<sup>2</sup>, Dimitris Visvikis<sup>1</sup>

<sup>1</sup> LaTIM, Inserm UMR 1101, University of Brest, Brest, France .

<sup>2</sup> Dept. Nuclear Medicine, Bern University Hospital, University of Bern, Bern, Switzerland .

\*Corresponding author(s). E-mail(s): [alexandre.bousse@univ-brest.fr](mailto:alexandre.bousse@univ-brest.fr);  
Contributing authors: [baptiste.laurent@univ-brest.fr](mailto:baptiste.laurent@univ-brest.fr);

## Abstract

**Objective:** Long-axial field-of-view (LAFOV) positron emission tomography (PET) systems allow higher sensitivity, with an increased number of detected lines of response induced by a larger angle of acceptance. However this extend angle increase the number of multiple scatters and the scatter contribution within oblique planes. As scattering affects both quality and quantification of the reconstructed image, it is crucial to correct this effect with more accurate methods than the state-of-the-art single scatter simulation (SSS) that can reach its limits with such an extended field-of-view (FOV). In this work, which is an extension of our previous assessment of deep learning-based scatter estimation (DLSE) carried out on a conventional PET system, we aim to evaluate the DLSE method performance on LAFOV total-body PET.

**Approach:** The proposed DLSE method based on a convolutional neural network (CNN) U-Net architecture uses emission and attenuation sinograms to estimate scatter sinogram. The network was trained from Monte-Carlo (MC) simulations of XCAT phantoms [<sup>18</sup>F]-FDG PET acquisitions using a Siemens Biograph Vision Quadra scanner model, with multiple morphologies and dose distributions. We firstly evaluated the method performance on simulated data in both sinogram and image domain by comparing it to the MC ground truth and SSS scatter sinograms. We then tested the method on 7 [<sup>18</sup>F]-FDG and 7 [<sup>18</sup>F]-PSMA clinical datasets, and compare it to SSS estimations.

**Results:** DLSE showed superior accuracy on phantom data, greater robustness to patient size and dose variations compared to SSS, and better lesion contrast recovery. It also yielded promising clinical results, improving lesion contrasts in [<sup>18</sup>F]-FDG datasets and performing consistently with [<sup>18</sup>F]-PSMA datasets despite no training with [<sup>18</sup>F]-PSMA.

**Significance:** LAFOV PET scatter can be accurately estimated from raw data using the proposed DLSE method.

**Keywords:** positron emission tomography (PET), scatter estimation, scatter correction, deep learning (DL), image reconstruction

## 1 Introduction

The emergence of long-axial field-of-view (LAFOV) positron emission tomography (PET)/computed tomography (CT) systems has led to significant

advancements in nuclear medicine, providing opportunities to new applications [1–5]. These systems provide extended body coverage and improved sensitivity, enabling reductions in either radiopharmaceutical doses or acquisition times [6]. However, despite

these advantages, the geometry of LAFOV PET systems is more prone to an increased impact of scatter coincidences due to the larger solid angle of acceptance resulting from the extended field of view. This presents challenges for data correction algorithms in terms of both qualitative and quantitative image accuracy.

Scatter coincidences, caused by Compton single or multiple interactions of one or both of the annihilation gamma photons with the attenuation medium, negatively impact quantification and degrade PET image quality. Therefore, scatter must be corrected during the reconstruction process. Traditionally, this is achieved through methods such as single scatter simulation (SSS) [7–9] and Monte-Carlo (MC) simulations [10–12]. The SSS approach, which is the most popular and widely used scatter correction in clinical practice, requires an additional scaling step for the single scatter estimation to account for the presence of multiple scatters. However, since the distribution of multiple scatters differs from that of single scatters [13], scaling the single scatter distribution cannot accurately account for multiple scatters nor activity from outside the FOV, leading to inaccuracies. To address this, double scatter simulation (DSS) algorithms have been developed, extending the simulation to include second-order scatters [13, 14]. However, these methods are generally limited to scatter estimation in direct planes or make less accurate estimation of oblique plane scatter contributions, which are much more prominent in LAFOV PET systems. In addition to variations in scatter distribution along the axial length of the system [15], it has been demonstrated that, in LAFOV PET systems, the scatter distribution also varies with the axial angle of the plane, as does the single-to-multiple scatter ratio [16]. Incorporating oblique planes into scatter estimation can therefore improve the robustness and accuracy of the scatter correction process [17].

MC-based methods provide highly accurate scatter estimations [18], but they are computationally intensive for clinical applications, particularly with LAFOV systems, where scatter estimation can take up to an hour per iteration [19].

Recent deep learning (DL) post-processing techniques aim at correcting scatter in the image domain by transforming uncorrected images into scatter-free ones [20, 21]. These methods benefit from shorter computation times and show promising results. However, they disregard important spatial information inherent to PET imaging physics, such as Compton scattering, and may introduce artefacts or bias directly into the final

image. In addition, as with most DL-based image generation approaches, such techniques lack in terms of generalisation and scanner independent applicability.

Within this context, the deep learning-based scatter estimation (DLSE) approach we proposed in [22] estimates three-dimensional (3D) scatter sinograms from 3D emission and attenuation sinograms. It has proven effective on conventional PET systems, delivering more robust and accurate results than SSS. The goal of this study was to evaluate its performance in addressing the specific challenges of scatter correction in LAFOV scanners.

The rest of this paper is organised as follows. Section 2 summarises the basics of PET image reconstruction with sinogram-based scatter correction using DLSE, as well as our evaluation strategy. Section 3 compares DLSE and SSS on simulated and patient data and the results are discussed in Section 4. Section 5 concludes this work.

## 2 Materials and Methods

### 2.1 Scatter-Corrected Image Reconstruction

Image reconstruction consists in estimating the radioactivity distribution image  $\mathbf{x} = [x_1, \dots, x_J]^\top \in \mathbb{R}^J$  from a measurement sinogram vector  $\mathbf{y} = [y_1, \dots, y_I]^\top \in \mathbb{R}^I$ , with  $I$  being the number of PET detector bins, and  $J$  the number of voxels in the final image. Given an activity distribution  $\mathbf{x}$ , the measurement vector  $\mathbf{y}$  follows a Poisson distribution with independent entries with expectation

$$\mathbb{E}[\mathbf{y}] = \bar{\mathbf{y}}(\mathbf{x}) \quad (1)$$

where  $\bar{\mathbf{y}}(\mathbf{x})$  is the PET forward model, traditionally defined as

$$\bar{\mathbf{y}}(\mathbf{x}) = \tau \mathbf{A} \mathbf{P} \mathbf{x} + \bar{\mathbf{r}} + \bar{\mathbf{s}} \quad (2)$$

where  $\tau$  is the acquisition time,  $\mathbf{A} = \text{diag}[\mathbf{a}] \in \mathbb{R}^{I \times I}$  is a diagonal matrix defined by the attenuation factors (AFs)  $\mathbf{a} = [a_1, \dots, a_I]^\top \in \mathbb{R}^I$ ,  $\mathbf{P} \in \mathbb{R}^{I \times J}$  is the PET system matrix defined as  $[\mathbf{P}]_{i,j} = p_{i,j}$  for all  $i, j$ ,  $\bar{\mathbf{r}} = [\bar{r}_1, \dots, \bar{r}_I]^\top \in \mathbb{R}^I$  is the expected random coincidences and  $\bar{\mathbf{s}} = [\bar{s}_1, \dots, \bar{s}_I]^\top \in \mathbb{R}^I$  is the expected scatter. The reconstruction of the image is achieved by finding an image  $\mathbf{x}$  such that  $\bar{\mathbf{y}}(\mathbf{x}) \approx \mathbf{y}$  in the sense of  $\mathbf{x}$  is a minimiser of the Poisson log-likelihood given the measurement sinogram  $\mathbf{y}$ .

The reconstruction is commonly achieved using the maximum-likelihood expectation-maximisation (EM) algorithm [23] or its accelerated version ordered-subset EM (OSEM) [24]. This requires an accurate knowledge of the hyper parameters of  $\bar{\mathbf{y}}$  in (2): the AFs  $\mathbf{a}$ , the expected randoms  $\bar{\mathbf{r}}$  and scatter  $\bar{\mathbf{s}}$ . The AFs  $\mathbf{a}$  are computed with a forward projection of the 511-keV attenuation map that is usually derived from a CT scan. Randoms can be corrected for by real-time subtraction of a delayed coincidence channel [25], and the scatter estimation in clinical systems is widely performed using the SSS approach. [7–9].

The DLSE method we introduced in our previous paper [22] aims to leverage the interrelation between emission, attenuation and scatter in order to estimate  $\bar{\mathbf{s}}$  from the measured sinogram data  $\mathbf{y}$  and AFs  $\mathbf{a}$  using a convolutional neural network (CNN)  $f_{\theta}$ . For practical purposes, we exploit the attenuation correction factors (ACFs)  $\mathbf{b} = [1/a_1, \dots, 1/a_I]^T$  instead of the AFs  $\mathbf{a}$ . The network  $f_{\theta}: \mathbb{R}^I \times \mathbb{R}^I \rightarrow \mathbb{R}^I$  is then trained such that

$$f_{\theta}(\mathbf{y}, \mathbf{b}) \approx \bar{\mathbf{s}} \quad (3)$$

where  $\theta$  is the vector of weights to be trained.

In the rest of this paper we assume that the emission data  $\mathbf{y}$  is random-free, i.e.,  $\bar{\mathbf{r}} = \mathbf{0}$ .

## 2.2 Network Architecture

The DLSE network  $f_{\theta}$  is based on a U-Net architecture [26]. It processes concatenated PET emission and ACF slices derived from a 3D sinogram with a dimension of  $520 \times 50 \times 11559$  (respectively corresponding to bin displacement, bin angle, and axial slice index) and produces predicted scatter sinogram slices. Each of the five layers of the network contains two  $3 \times 3$  convolutional layers followed by a rectified linear unit activation function and  $2 \times 2$  max pooling. To prevent overfitting, dropout layers are added at the end of the contraction path. The expansion path is similar to the contraction path but replaces max pooling with  $2 \times 2$  nearest-neighbour up-sampling to preserve the initial sinogram dimensions. The network ensures that the output dimensions match those of the input sinograms. The architecture is shown in Figure 1.

The CNN was implemented using the Keras framework [27] with a TensorFlow back-end [28].

## 2.3 Training

The data used for training the network consists exclusively of MC simulations generated from radiotracer

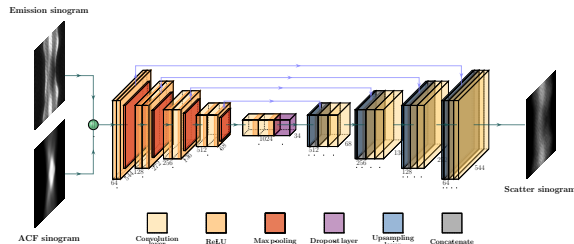


**Fig. 1:** Proposed DLSE architecture based on a CNN U-Net architecture. The network takes emission and attenuation sinograms as input and predicts the scatter sinogram.

distribution and morphologies. For each experiment, we used a collection of  $P$  MC-simulated random-free PET emission sinograms  $\mathbf{y}$  and scatter sinograms  $\mathbf{s}$  as well as the corresponding ACFs  $\mathbf{b}$ . The training of  $\theta$  is achieved via the minimisation problem

$$\min_{\theta} \mathbb{E} [\mathcal{L}(f_{\theta}(\mathbf{y}, \mathbf{b}), \mathbf{s})] \quad (4)$$

where the expectation is taken over the  $P$  realisations of  $(\mathbf{y}, \mathbf{b}, \mathbf{s})$  and  $\mathcal{L}$  is a loss function we defined as the mean squared error (MSE), i.e.,

$$\mathcal{L}(\mathbf{u}, \mathbf{v}) = \frac{1}{I} \|\mathbf{u} - \mathbf{v}\|_2^2, \quad (5)$$

$\|\cdot\|_2$  being the Euclidian norm.

Note that the forward model (2) utilises the *expected* scatter sinograms  $\bar{\mathbf{s}}$  while we train our model with MC-simulated sinograms  $\mathbf{s}$ . In principle, the model should be trained with the expected scatter sinograms  $\bar{\mathbf{s}} = \mathbb{E}[\mathbf{s}]$  obtained by averaging several MC instances of  $\mathbf{s}$ . However, due to the high computational time, we only used a single instance of  $\mathbf{s}$  and we assumed  $\mathbf{s} \approx \bar{\mathbf{s}}$ . In the following  $\mathbf{s}$  will be referred to as the ground truth (GT).

The sinograms were normalised for training such that  $\mathbf{y}$ ,  $\mathbf{b}$  and  $\mathbf{s}$  range between 0 and 1. The output of DLSE were then denormalised. We also resized using zero padding so that their dimension is a multiple of  $2^5$ , five being the number of convolution steps of the network.

The Adam optimiser [29] was used to train the model by solving (4) for 10 epochs and with a learning rate of  $10^{-5}$  as well as a batch size of eight.

## 2.4 Data Generation

In this section we describe how generated the 3-tuple  $(\mathbf{y}, \mathbf{b}, \mathbf{s})$  used to perform the network training (4).

### 2.4.1 Phantom Generation

We used the extended cardiac-torso (XCAT) phantom [30] to produce radiotracer distribution and attenuation maps. As scatters can be affected by object size [31], three different morphologies (Table 1) were generated. [ $^{18}\text{F}$ ]-fluorodeoxyglucose ([ $^{18}\text{F}$ ]-FDG) activity distributions were then attributed to each organ of the anatomical maps, with distributions inspired from the literature [32]. The activity and associated 511-keV attenuation maps, used to derive the ACFs, consist of  $312 \times 312 \times 200$  images with a  $2 \times 2 \times 2\text{-mm}^3$  voxel size. In order to include scatter from outside the scanner’s axial field-of-view (FOV), the activity along the whole phantom’s length was considered for the simulation. Multiple radiotracer doses were used to obtain a representative training dataset of realistic PET acquisitions. More specifically, five additional activity distributions were defined by increasing the reference activity by 10%, 20% and 30% as well as reducing it by 10% and 20%. For each labelled organ, we added a  $\delta$  activity to these new defined distributions, which is randomly set between -5% and +5%, to introduce activity variability from organ to organ. These different activity distributions were considered for each of the three different anatomical morphologies.

	Small	Medium	Large
Total body height (mm)	1,227	1,752	2,103
Chest short axis (AP) (mm)	163	232	279
Chest Long axis (LAT) (mm)	228	325	391
Chest circumference (mm)	696	993	1,194
Waist short axis (AP) (mm)	163	233	335
Waist long axis (LAT) (mm)	202	288	416
Body weight (kgs)	28	76	129
Body mass index (BMI) (kg/m <sup>2</sup> )	18.6	24.8	29.2
Radiotracer standard dose (MBq)	50	141	239

**Table 1:** Anatomical characteristics of the three simulated phantom morphologies.

### 2.4.2 Monte-Carlo Simulations

Monte Carlo (MC) tools have been shown to accurately simulate the Siemens Vision 600 and the Vision Quadra scanner models, as evidenced by their good

Ring diameter	82 cm
Transaxial FOV	726 mm
Axial FOV	106 cm
Crystal material	LSO
Crystal dimensions	$3.2 \times 3.2 \times 20$ mm
Total number of crystals	243,200
Crystal Rings	320
Crystals per ring	760
Crystals per detector block	64 (8 $\times$ 8)
Energy window	435–585 keV
Coincidence window	4.7 ns

**Table 2:** Siemens Vision Quadra characteristics [5].

agreement with experimental data [33, 34]. The Vision Quadra model geometry within the Geant4 Application for Tomography Emission (GATE) software [35] consists of four Siemens Vision 600 units aligned with an axial gap between them.

We performed MC simulations using the XCAT-generated phantoms and the GATE software to simulate data acquisition on the Siemens Biograph Vision Quadra PET scanner [5] (characteristics shown in Table 2). The simulations were handled using back-to-back gamma photons sources, generated from the three distinct morphologies and six varied activity distributions, as described in the previous section, resulting in a total of 18 simulations.

The number of coincidences of the simulated measurement sinograms varied from  $0.44 \times 10^9$  to  $2.40 \times 10^9$ , with a mean of  $1.2 \pm 0.55 \times 10^9$ , with a mean scatter ratio of 31.5% with a minimum of 26.7% (for the small phantom with a body mass index (BMI) of 18.6) up to 34.6% (for the large phantom with a BMI of 29.9). These scatter fractions as a function of BMI correspond well with those shown previously in the literature [36]. The single scatters contribution reached a ratio of 28.1% (from 24.4% to 30.5%) while the mean multiple scatters reached 3.4% (from 2.2% to 4.2%).

Each activity, scatter and ACF sinogram consists of 11,559 sinograms slices (with dimensions of  $520 \times 50$ ), which represents a total of  $P = 208,062$  realisations of  $(\mathbf{y}, \mathbf{b}, \mathbf{s})$ , allocated as follows: 2/3 for training, 1/6 for validation and 1/6 for testing.

## 2.5 Evaluation on Simulated Data

The phantoms used for evaluation were not included in the training. DLSE scatter sinograms were compared to the MC GT and SSS scatter sinograms. In addition to visualising scatter distributions and profile lines, we used normalised root mean squared error (NRMSE)

to evaluate its robustness according to patient size and injected dose variations, with NRMSE defined as

$$\text{NRMSE}(\hat{s}, s) = \frac{\mathcal{L}(\hat{s}, s)}{\hat{s}_{\max} - \hat{s}_{\min}} \quad (6)$$

where  $s$  is the MC GT sinogram and  $\hat{s}$  is the estimated one (by either DLSE or SSS),  $\hat{s}_{\max}$  and  $\hat{s}_{\min}$  being respectfully the maximal and minimal values of  $\hat{s}$ , and  $\mathcal{L}$  is the MSE loss defined in (5).

We then performed an evaluation in the image domain, after a reconstruction of the sinograms with OSEM (3 iterations, 24 subsets) using Siemens e7tools toolkit. Images were reconstructed into a  $440 \times 440 \times 645$  matrix with 1.65-mm cubic voxels. MC GT and DLSE sinograms were smoothed by a 4-mm-full width at half maximum (FWHM) Gaussian filter before being injected into the forward model  $\bar{y}$  used for reconstruction (i.e., the expected scatter  $\bar{s}$  in (2)).

We evaluated the DLSE performance in various organs, by defining four 50-mm-diameter spherical regions of interest (ROIs), in which we compute the mean standardised uptake value activity error. We finally simulated a phantom incorporating six spherical lesions of various sizes (10-mm, 20-mm and 40-mm) and locations (three in the lungs, three in the liver) to assess the DLSE performance when faced with cold or hot abnormal activities. The simulation was performed for three lesion contrasts, 0:1, 3:1 and 6:1, where the contrast is computed as

$$\text{lesion contrast} = \frac{\text{mean lesion activity}}{\text{mean organ activity}} \quad (7)$$

## 2.6 Evaluation on Clinical Data

In a first step, we used seven  $^{18}\text{F}$ -FDG clinical datasets acquired with a Vision Quadra total body scanner to assess the DLSE performance on real clinical data. The 10 minutes acquisitions, with patient weights ranging from 52 to 98 kgs and mean injected dose ranging from 160 to 297 MBq, led to a detected coincidences count varying from  $2.5 \times 10^9$  to  $4.7 \times 10^9$ . The data were reconstructed using the same process as described in Section 2.5. We subsequently compared mean activities within multiple regions of interest of DLSE and SSS corrected PET images.

In addition, we applied our  $^{18}\text{F}$ -FDG-trained DLSE model to seven  $^{18}\text{F}$ -prostate-specific membrane antigen-11 ( $^{18}\text{F}$ -PSMA) clinical datasets. The patients' mean weights ranged from 51 to 98kg, with mean injected doses between 197 and 204 MBq. The

	$^{18}\text{F}$ -FDG	$^{18}\text{F}$ -PSMA
Patient weight (kgs)	$77.6 \pm 15.1$	$74.4 \pm 13.6$
Body mass index (BMI) ( $\text{kg}/\text{m}^2$ )	$26.6 \pm 6.38$	$25.0 \pm 3.52$
Injected activity (MBq)	$233.4 \pm 45.5$	$199.7 \pm 2.4$
Coincidences ( $\times 10^9$ )	$3.6 \pm 0.6$	$0.8 \pm 0.2$

**Table 3:** Clinical acquisition characteristics.

four minutes acquisitions provided from  $579 \times 10^6$  up to  $1\,038 \times 10^6$  detected coincidences. This assessment aimed to evaluate the capability of the DLSE approach to generalise across various radiopharmaceuticals beyond those included in its training. Our analysis focused particularly on prostate lesions and associated metastases, comparing the resulting activity levels in PET images corrected by DLSE and SSS.

The characteristics of the acquisition are summarised in Table 3.

## 3 Results

### 3.1 Simulated Data

In the following results reporting, the metrics are averaged over the testing dataset. For example, the NRMSE on the small phantom is averaged over all doses, while the NRMSE for a given dose is averaged over all phantom sizes.

#### 3.1.1 Scatter Sinograms Estimation

In this section we compare the performances of DLSE and SSS for the estimation of  $s$ . The NRMSE is computed between the estimated scatter  $\hat{s}$  and the GT scatter  $s$ .

Figure 2 shows the emission sinogram  $y$ , the ACFs  $b$ , the GT scatter  $s$ , and the outputs of DLSE and SSS (scatter sinograms were smoothed using a 4-mm FWHM Gaussian filter) under two conditions: (i) a low-dose setting (standard dose  $-20\%$ , see Table 1 for the standard dose) with a small phantom, and (ii) a high-dose setting (standard dose  $+30\%$ ) with a large phantom. The DLSE scatter sinogram distribution resembles qualitatively the GT in both settings, with no visible artefacts. In the small phantom scenario, the scatter profiles show that the DLSE scatter distribution aligns closely with the GT on the tails, although the activity peak is slightly underestimated. In contrast, SSS exhibits some errors on the tails but accurately matches the maximum scattered activity. On the other hand, in the large phantom example, SSS

underestimates scatter activity, whereas DLSE more closely approximates the GT.

Figure 3 presents the NRMSE between the GT scatter  $s$  and the estimated scatter  $\hat{s}$  across various phantom sizes and doses. We observe that DLSE outperforms SSS in both experiments. DLSE appears to be less sensitive to the phantom size than SSS, with NRMSE ranging from  $0.153 \pm 0.016$  to  $0.163 \pm 0.014$  for DLSE and from  $0.215 \pm 0.012$  to  $0.243 \pm 0.020$  for SSS. We also note that the performance of DLSE improves gradually with increasing injected dose, with NRMSE ranging from  $0.184 \pm 0.005$  to  $0.137 \pm 0.009$ . In contrast, the accuracy of SSS slightly decreases with increasing injected dose, where the NRMSE ranges from  $0.217 \pm 0.016$  to  $0.238 \pm 0.024$ .

### 3.1.2 Reconstructed Images

The next analysis is conducted on reconstructed images from MC simulated data  $y$  using the reconstruction process described in Section 2.5 and estimated scatter  $\hat{s}$  obtained from DLSE and SSS.

Figure 4 shows the reconstructed images with and without scatter correction. The image reconstructed from scatter-free data is referred to as the “reference image”. The DLSE-scatter corrected images are visually similar to the MC GT and display no artefacts. The profile analysis demonstrates that DLSE-corrected images yield more accurate estimates of activity in the 10-mm liver lesion with a 6:1 contrast (first row). In this case, SSS correction underestimates the lesion activity due to an overestimation of scatter contribution within the region. Overall, the DLSE profile line aligns more closely with the reference image compared to the SSS correction. In the profile lines of the second row, representing a 20-mm lung lesion with a 3:1 contrast, both correction methods lead to an accurate estimate of the lesion maximum standardised uptake value (SUV<sub>max</sub>) value. However, the SSS correction underestimates activity in the lung region, particularly in the trachea. A similar pattern is observed in the profile lines of the final row, which depict a necrotic 40-mm lung lesion (0:1 contrast). SSS correction tends to over-correct for scatter in lungs and trachea, although it performs well in the shoulder region. The DLSE profile line shows good agreement with the reference image but exhibits an activity overestimation in the area between the lesion and the heart.

Figure 5 shows the NRMSE results for DLSE- and SSS-corrected reconstructed images, computed using the scatter-free reconstructed image as a reference. We

observe that performance decreases for both methods as the phantom size increases. DLSE outperforms SSS across all phantom sizes, with NRMSE ranging from  $0.106 \pm 0.005$  to  $0.267 \pm 0.014$  for DLSE and from  $0.108 \pm 0.007$  to  $0.319 \pm 0.022$  for SSS. We also observe that performance improves with the injected dose for both methods, with DLSE again outperforming SSS at all dose levels, confirming the results shown in Figure 3b. For DLSE, the NRMSE decreases from  $0.199 \pm 0.088$  to  $0.176 \pm 0.073$ , while for SSS, it decreases from  $0.231 \pm 0.117$  to  $0.192 \pm 0.096$ .

Figure 6 shows quantitative results in the reconstructed images over different ROIs. Figure 6a shows the NRMSE on specific organs. While both DLSE and SSS methods shows similar NRMSE on liver region ( $6.30 \pm 4.74$  versus  $7.09 \pm 6.53$ ), DLSE outperforms SSS on lungs ( $2.21 \pm 1.21$  versus  $5.66 \pm 3.40$  for right lung and  $2.83 \pm 1.72$  versus  $5.23 \pm 3.30$  for left lung), and brain regions ( $0.31 \pm 0.34$  versus  $3.40 \pm 3.38$ ). Figure 6b shows the contrast on the three lesions (0:1, 3:1 and 6:1) for the reference image, and DLSE SSS-corrected images, computed following (7). DLSE yields closer lesion contrasts to the reference image than SSS, regardless of the simulated contrast. For necrosed lesions, with a contrast of 0:1, the mean lesion contrasts in the reconstructed image are respectively, 0.649, 0.657 and 0.649 for DLSE, SSS and reference methods. At a 3:1 contrast, the values are 1.611, 1.778, and 1.657, and at a 6:1 contrast, they are 2.400, 2.657, and 2.459, respectively.

## 3.2 Clinical Data

### 3.2.1 FDG Datasets

Figure 7 shows three clinical [<sup>18</sup>F]-FDG dataset examples. The DLSE-corrected images are visually very similar to the SSS-corrected images. Examining the profile lines in the first row, which displays a breast lesion in a female patient, reveals similar patterns to those observed in the simulated images in Figure 4, with lower activity in the region between the lungs using SSS compared to DLSE. However, the activities within the lesion are very similar for both DLSE and SSS.

In the second row dataset, DLSE provides better contrast on the nodules than SSS, showing similar activity levels between the nodules but with a higher activity peak.

The last dataset shows kidney structures in a large morphology patient (98 kg). The SSS-corrected image

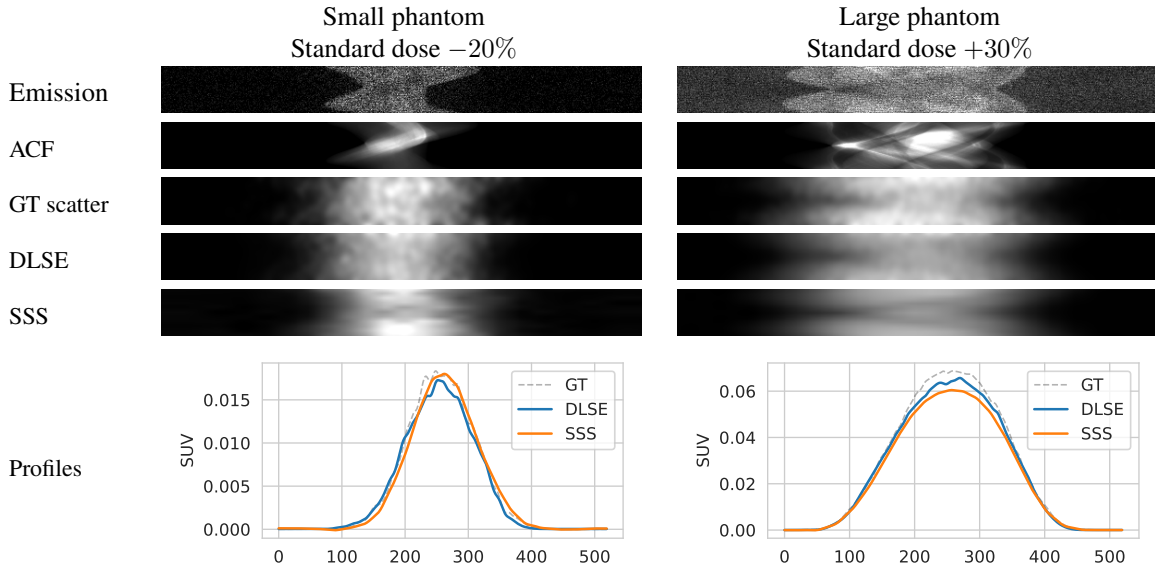


**Fig. 2:** Input activity and attenuation sinograms, followed by GT, DLSE and SSS scatter sinograms as well as their profile lines along the bins axis.

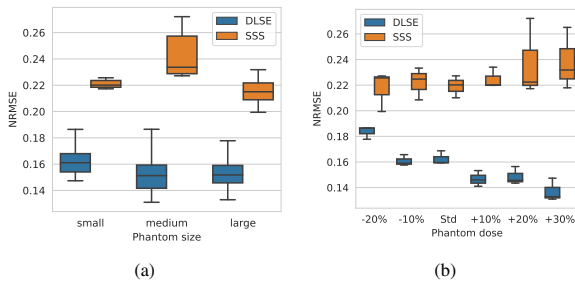


**Fig. 3:** NRMSE of the DLSE- and SSS-estimated sinograms according to (a) the phantoms size and (b) the dose.

exhibits an overall higher activity than the DLSE-corrected image. After manual segmentation of the kidneys and automatic segmentation of its structures using the FLAB algorithm [37], the contrast is found to be slightly higher in the DLSE corrected PET images. The contrast is 2.3 with DLSE correction, compared to 2.2 with SSS correction and 1.8 in the uncorrected image.

Figure 8 shows the correlation between activities in DLSE- and SSS-corrected PET images across different organs. Considering all ROIs, the relationship between the mean activities of both methods is given by the regression function  $y = 1.03x + 0.08$ . Activity values

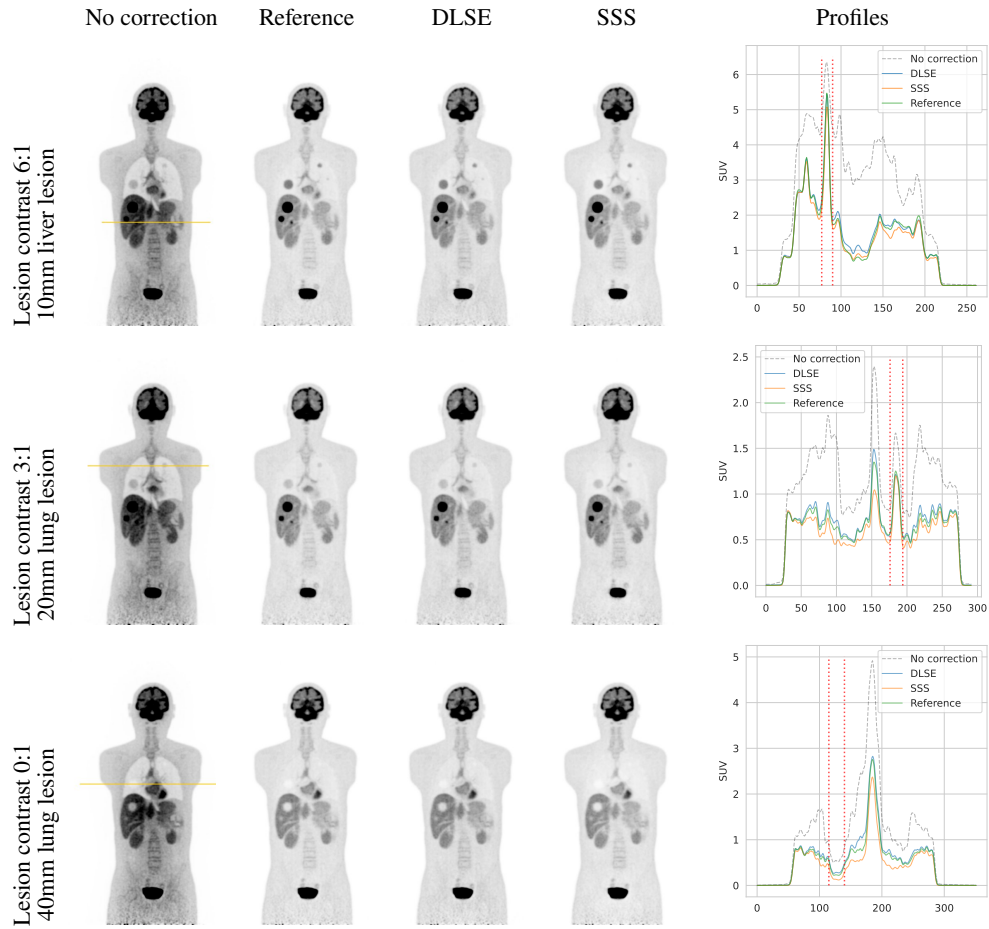
are similar in the brain and lung regions, but DLSE-corrected images tend to show higher activity levels in the liver compared to SSS-corrected images.

### 3.2.2 PSMA Datasets

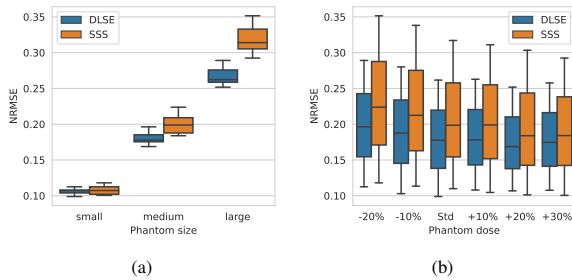
In this section, we present the results of our  $[^{18}\text{F}]$ -FDG-trained DLSE model applied to  $[^{18}\text{F}]$ -PSMA to evaluate its ability to generalise to radiotracers not included in the training data.

Figure 9 shows two clinical  $[^{18}\text{F}]$ -PSMA dataset examples. The first dataset illustrates a patient with a prostate lesion and shows good agreement between the DLSE and SSS corrected PET images for both the organs and the lesion.

The second patient example features two adjacent liver lesions; one with a higher and one with a lower activity level compared to the background liver activity. The DLSE-corrected image shows higher activity levels in both the liver and the lesions. Based on a 3D manual segmentation of the liver and the FLAB segmentation of the lesions, the contrast values were found to be similar for DLSE and SSS, with values of 0.87 and 0.86, respectively, for the necrotising lesion, and 1.64 and 1.67, respectively, for the active lesion. These values compare with contrasts of 0.92 and 1.53, respectively, in the non-scatter-corrected image.



**Fig. 4:** Reconstructed images using simulated data without and with scatter correction using SSS and DLSE corrections. The reference image corresponds to the reconstruction from scatter-free data. Profile are shown along the yellow lines drawn of the first column. Lesion borders are represented with the vertical dashed red lines.



**Fig. 5:** NRMSE of the DLSE- and SSS-reconstructed images according to (a) the phantom size (b) and (b) the dose.

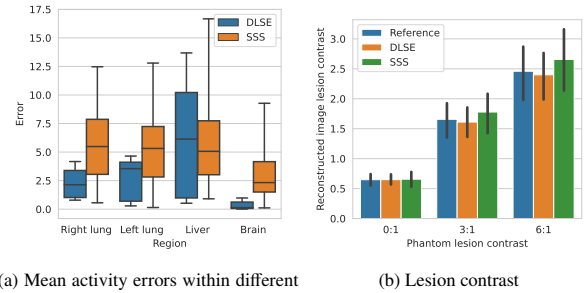
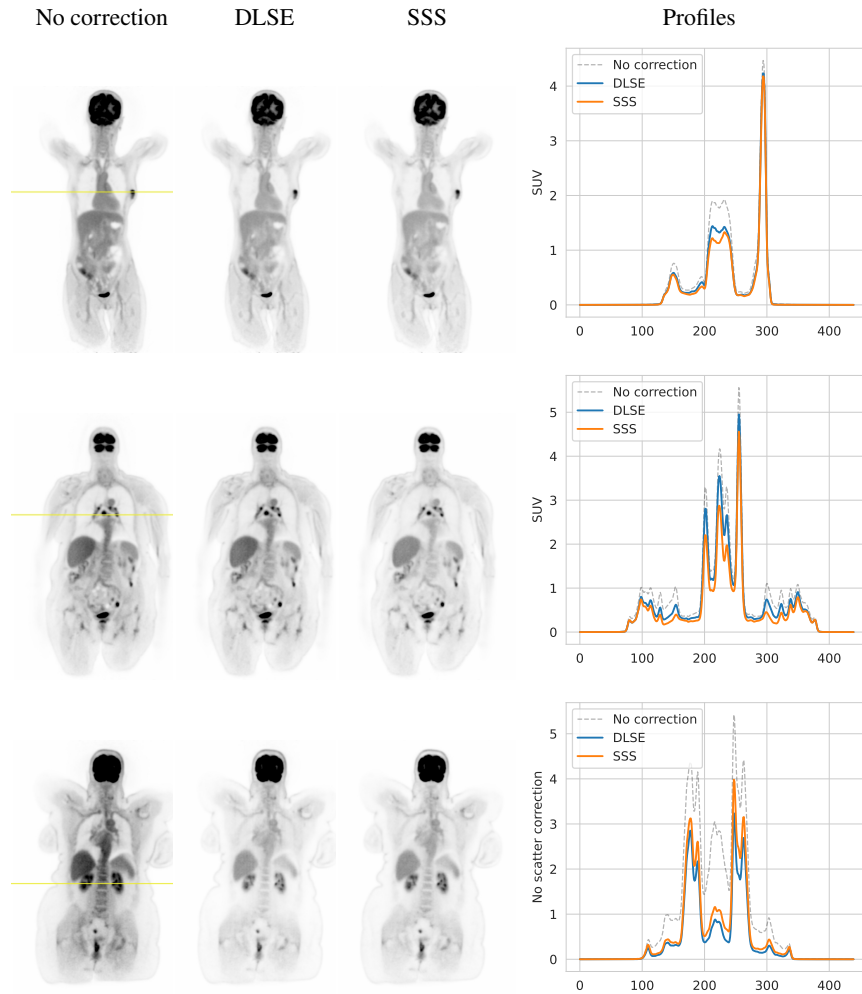


**Fig. 6:** DLSE and SSS reconstructed images results for different (a) ROIs and (b) lesion contrasts.

Figure 10 displays the correlation between DLSE and SSS SUVmax values for lesions in the  $[^{18}\text{F}]$ -PSMA dataset, highlighting good agreement between

the two methods, with a relationship defined by the affine function  $y = 0.97x + 0.24$ .





	Sex	Weight	Dose	Coincidences
1st row	Female	52 kgs	160 MBq	3.0 billions
2nd row	Male	80 kgs	244 MBq	4.7 billions
3rd row	Female	98 kgs	297 MBq	3.8 billions

**Fig. 7:** Clinical  $[^{18}\text{F}]$ -FDG data reconstructed without scatter correction as well as with DLSE and SSS corrections. Profile are shown along the yellow lines drawn of the first column. The same contrast is applied to the three images of a single row.

### 3.3 Computational Speed

The DLSE method was run on an Intel Xeon 3.70 Ghz 10-core CPU and NVIDIA RTX A6000 GPU. The learning step took two hours per epoch resulting in 20 hours for the whole training process. The prediction of a whole 3D scatter sinogram of 11,559 slices takes 381 seconds (33 ms per sinogram slice).

## 4 Discussion

This study aims to assess the performance of a previously proposed deep learning scatter estimation method, DLSE, using raw PET data in the context of LAFOV systems. It is worth noting that the training of the proposed DLSE approach is entirely based on the use of simulated datasets, hence removing

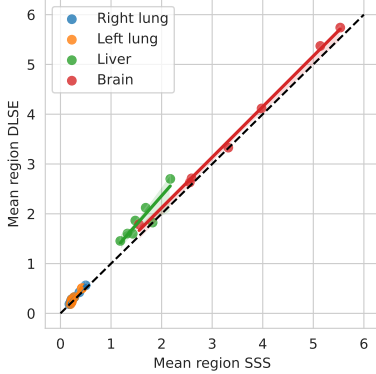


**Fig. 8:** Mean standardised uptake value correlation between DLSE and SSS-corrected images within different organs

the need for clinical datasets in the training process. The first step involved evaluating the method on simulated images, allowing for comparison with the ground truth in both the sinogram and image domains. In the second step, DLSE was tested on 14 clinical datasets, encompassing a range of patient morphologies, tumour sizes, and locations, as well as two different radiopharmaceuticals.

The sinograms produced by DLSE from simulated datasets are visually similar to the ground truth and exhibit comparable distributions (Figure 2). DLSE also demonstrates better scatter quantification than the SSS sinogram, particularly for larger phantoms, where SSS tends to underestimate scatter levels. This underestimation is more likely in cases of large morphologies that occupy a significant portion of the system’s FOV, leading to inaccuracies in the tail-fitting scale factor used to account for multiple scatter events. The results shown in Figure 3 confirm that the scatter sinograms produced by DLSE are more accurate and less sensitive to phantom size and dose than SSS-produced sinograms.

Reconstruction of simulated data corrected with DLSE closely resembles the reference image, exhibiting no significant artefacts in various organs or around the lesions (Figure 4). In addition to demonstrating better robustness to phantom size, the quantitative analysis reveals that DLSE is more resilient to variations in injected dose levels, showing lower NRMSE disparity compared to SSS in the reconstructed PET images (Figure 5b). In addition to demonstrating better robustness to phantom size, DLSE provides better accuracy than SSS on all considered doses. The performance

of DLSE consistently improves as the patient activity increases but it decreases as the patient size increases (Figure 5a and Figure 5b). Furthermore, the analysis of different organ activities (Figure 6a) indicates an improved accuracy for low-activity regions, such as lungs, as well as for high-activity brain region. DLSE also proved to be more accurate, providing closer contrast recovery than SSS, when compared to reference image lesion contrasts (Figure 6b).

The study conducted on clinical [ $^{18}\text{F}$ ]-FDG acquisitions demonstrated consistent results for DLSE, producing visually comparable outcomes to SSS-corrected images (Figure 7). The method appeared to be robust against significant variations in patient morphology, with weights ranging from 52 to 98 kg. In two of the three cases, DLSE-corrected images exhibited slightly higher activity levels, while the SSS method showed higher activity in the large morphology patient. This discrepancy may be attributed to inaccuracies in the tail-fitting algorithm used to estimate the scaling factor for multiple scatters, as the tails could potentially be too small for larger morphology patients. In all three examples, the lesion contrasts were found to be greater than those obtained with the SSS-based scatter correction.

It is also worth noting that the acquisition duration for these clinical datasets is twice as long as that of the simulated training data (six minutes compared to three minutes). These longer acquisition times naturally result in a higher number of detected coincidences, with a mean of  $1.2 \pm 0.55 \times 10^9$  for the simulated dataset, compared to a mean of  $3.6 \pm 0.6 \times 10^9$  coincidences for the [ $^{18}\text{F}$ ]-FDG datasets. Consequently, the method is capable of adapting to different statistical levels in the data, which may arise from variations in radiopharmaceutical doses or acquisition durations.

Finally, Figure 9 shows visually similar results between DLSE and SSS-corrected images. Furthermore, SUVmax values were found to be similar between the two methods (Figure 10). These results suggest that the method could adapt from one radiopharmaceutical to another without the need for retraining.

The prediction of the 3D scatter sinogram takes about 380 seconds. In comparison, the SSS 3D scatter estimation requires approximately 100 seconds, while the DSS can take an average of 5.9 times longer than the SSS on systems with a large number of time-of-flight (TOF) bins [14]. The speed performance of DLSE can be significantly improved by reducing the resolution of the input scatter sinograms. Specifically, the output

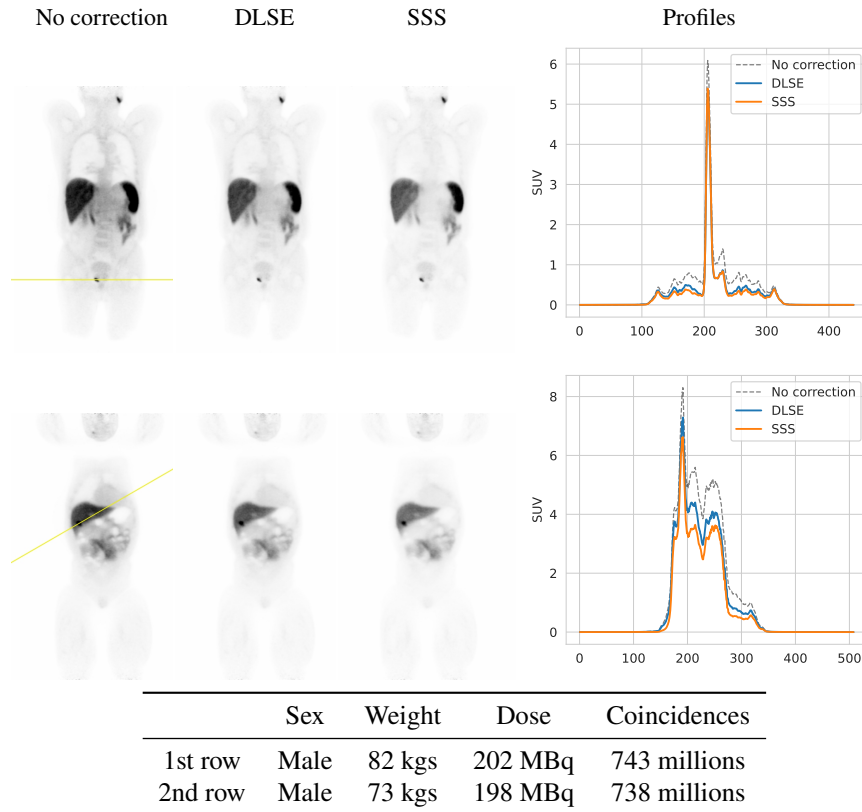


**Fig. 9:** Clinical  $[^{18}\text{F}]$ -PSMA data reconstructed without scatter correction as well as with DLSE and SSS corrections. Profile are shown along the yellow lines drawn of the first column. The same contrast is applied to the 3 images of a single row.

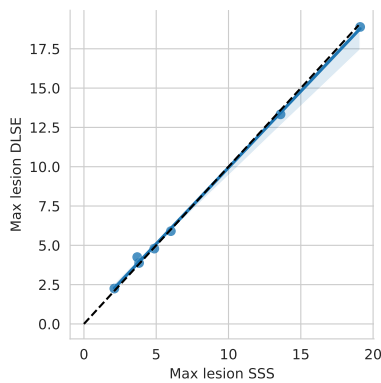


**Fig. 10:** DLSE and SSS-corrected images SUVmax correlation within lesions of  $[^{18}\text{F}]$ -PSMA dataset

scatter sinogram is smoothed with a Gaussian filter before being incorporated into the reconstruction. For this study and the resulting qualitative and quantitative sinogram analysis, we opted to maintain the original

sinogram dimensions. However, the pre-reconstruction smoothing step could be replaced with sinogram down-sampling prior to network training without losing significant information in the final scatter sinogram. Reducing the resolution by a factor of 2 in each dimension would yield a level of detail comparable to that of the Gaussian-smoothed sinogram, and would decrease the scatter estimation duration to under 50 seconds.

Realistic MC PET simulations are very computationally demanding; however, in the context of a DL-based method that utilises simulated data for training, the simulation processes only need to be run once.

Finally, the presented work has been applied to non-TOF PET data. A straightforward approach for adapting the method to TOF data, which represents a potential direction for future investigations, involves applying the method to each time bin sinogram.

## 5 Conclusions

In the present study we assessed the DLSE method on a clinical LAFOV PET system, representing more challenging scatter conditions compared to standard FOV PET scanners. This method offers the advantage of directly incorporating multiple scatters and oblique planes in the data correction process. Similarly with the performance previously shown on conventional PET systems, DLSE demonstrated higher accuracy on phantom data, demonstrating better robustness to variations in patient size and injected dose levels in comparison to SSS, also providing better lesion contrast recovery. DLSE also yielded high-quality results on clinical data, showing improved lesion contrasts on [<sup>18</sup>F]-FDG datasets and consistent results on [<sup>18</sup>F]-PSMA datasets, despite [<sup>18</sup>F]-PSMA activity distributions not being used during the DLSE training process. This study indicates that deep-learning methods applied to raw PET data are effective for scatter estimation and correction in LAFOV PET systems. Future investigations could focus on DLSE generalisation across multiple scanner geometries without requiring retraining.

## Statements & Declarations

### *Acknowledgments*

The authors would like to thank Jorge Cabello from Siemens Healthineers for sharing their tool for generating Siemens-format list-mode files from simulation files.

### *Funding*

The authors declare that no funds, grants, or other support were received during the preparation of this manuscript.

### *Competing Interests*

The authors have no relevant financial or non-financial interests to disclose.

### *Author Contributions*

All authors contributed to the study conception and design. Material preparation, data collection and analysis were performed by Baptiste Laurent. The first draft of the manuscript was written by Baptiste Laurent and Alexandre Bousse. The clinical data were prepared by Kuangyu Shi and Alex Rominger. The data converter used to convert Monte-Carlo simulations output files

to Siemens list-mode files format was developed by Jorge Cabello. All authors read and approved the final manuscript.

### *Data Availability*

The datasets generated during and/or analysed during the current study are available from the corresponding author on reasonable request.

### *Ethics approval*

This research does not involve human subjects—patient data were used retrospectively.

## References

- [1] Alberts, I., Sari, H., Mingels, C., Afshar-Oromieh, A., Pyka, T., Shi, K., Rominger, A.: Long-axial field-of-view PET/CT: perspectives and review of a revolutionary development in nuclear medicine based on clinical experience in over 7000 patients. *Cancer imaging : the official publication of the International Cancer Imaging Society* **23**, 28 (2023) <https://doi.org/10.1186/s40644-023-00540-3>
- [2] Slart, R., Tsoumpas, C., Glaudemans, A., Noordzij, W., Willemsen, A., Borra, R., Dierckx, R., Lammertsma, A.: Long axial field of view PET scanners: a road map to implementation and new possibilities. *European Journal of Nuclear Medicine and Molecular Imaging* **48** (2021) <https://doi.org/10.1007/s00259-021-05461-6>
- [3] Surti, S., Pantel, A.R., Karp, J.S.: Total body pet: Why, how, what for? *IEEE Transactions on Radiation and Plasma Medical Sciences* **4**(3), 283–292 (2020) <https://doi.org/10.1109/TRPMS.2020.2985403>
- [4] Alberts, I., Hünermund, J.-N., Prenosil, G., Mingels, C., Bohn, K., Viscione, M., Sari, H., Vollnberg, B., Shi, K., Afshar-Oromieh, A., Rominger, A.: Clinical performance of long axial field of view pet/ct: a head-to-head intra-individual comparison of the biograph vision quadra with the biograph vision pet/ct. *European Journal of Nuclear Medicine and Molecular Imaging* **48**, 1–10 (2021) <https://doi.org/10.1007/s00259-021-05282-7>

- [5] Prenosil, G., Sari, H., Fuerstner, M., Afshar-Oromieh, A., Shi, K., Rominger, A., Hentschel, M.: Performance characteristics of the biograph vision quadra pet/ct system with long axial field of view using the nema nu 2-2018 standard. *Journal of Nuclear Medicine* **63**, 121–261972 (2021) <https://doi.org/10.2967/jnumed.121.261972>
- [6] Mingels, C., Weidner, S., Sari, H., Buesser, D., Zeimpekis, K., Shi, K., Alberts, I., Rominger, A.: Impact of the new ultra-high sensitivity mode in a long axial field-of-view PET/CT. *Annals of nuclear medicine* **37** (2023) <https://doi.org/10.1007/s12149-023-01827-y>
- [7] Ollinger, J.: Model-based scatter correction for fully 3D PET. *Physics in medicine and biology* **41**, 153–176 (1996)
- [8] Watson, C.C., Newport, D., Casey, M.E.: A Single Scatter Simulation Technique for Scatter Correction in 3D PET, pp. 255–268. Springer, Dordrecht (1996)
- [9] Watson, C.C.: New, faster, image-based scatter correction for 3D PET. *IEEE Transactions on Nuclear Science* **47**(4), 1587–1594 (2000) <https://doi.org/10.1109/23.873020>
- [10] Barret, O., Carpenter, T., Clark, J., Ansorge, R., Fryer, T.: Monte Carlo simulation and scatter correction of the GE advance PET scanner with SimSET and Geant4. *Physics in medicine and biology* **50**, 4823–40 (2005) <https://doi.org/10.1088/0031-9155/50/20/006>
- [11] Holdsworth, C.H., Levin, C., Janecek, M., Dahlbom, M., Hoffman, E.J.: Performance analysis of an improved 3-d pet monte carlo simulation and scatter correction. *Nuclear Science, IEEE Transactions on* **49**, 83–89 (2002) <https://doi.org/10.1109/TNS.2002.998686>
- [12] Levin, C., Dahlbom, M., Hoffman, E.J.: A Monte Carlo correction for the effect of compton scattering in 3-D PET brain imaging. *Nuclear Science, IEEE Transactions on* **42**, 1181–1185 (1995) <https://doi.org/10.1109/23.467880>
- [13] Tsoumpas, C., Aguiar, P., Ros, D., Dikaios, N., Thielemans, K.: Scatter Simulation Including Double Scatter, vol. 3, pp. 1615–1619. *IEEE, ???* (2005). <https://doi.org/10.1109/NSSMIC.2005.1596628>
- [14] Watson, C.C., Hu, J., Zhou, C.: Double scatter simulation for more accurate image reconstruction in positron emission tomography. *IEEE Transactions on Radiation and Plasma Medical Sciences* **4**(5), 570–584 (2020) <https://doi.org/10.1109/TRPMS.2020.2990335>
- [15] Adam, L.-E., Karp, J.S., Brix, G.: Investigation of scattered radiation in 3D whole-body positron emission tomography using Monte Carlo simulations. *Physics in Medicine & Biology* **44**, 2879–2895 (1999)
- [16] Zhang, X., Zhou, J., Cherry, S., Badawi, R., Qi, J.: Quantitative image reconstruction for total-body PET imaging using the 2-meter long EXPLORER scanner. *Physics in Medicine and Biology* **62**, 2465–2485 (2017) <https://doi.org/10.1088/1361-6560/aa5e46>
- [17] Bal, H., Panin, V.Y., Schaefferkoetter, J., Cabello, J., Conti, M.: Fully 3D scatter estimation in axially long FOV PETCT scanners: Residual estimation approach. In: 2021 IEEE Nuclear Science Symposium and Medical Imaging Conference (NSS/MIC), pp. 1–4 (2021). <https://doi.org/10.1109/NSS/MIC44867.2021.9875665>
- [18] Teuho, J., Johansson, J., Linden, J., Saunavaara, V., Teräs, M.: Comparison of single-scatter simulation and Monte Carlo single-scatter simulation on Philips Ingenuity TF PET/MR. In: 2014 IEEE Nuclear Science Symposium and Medical Imaging Conference (NSS/MIC), pp. 1–3 (2014). <https://doi.org/10.1109/NSSMIC.2014.7430940>
- [19] Bayerlein, R., Spencer, B., Leung, E., Omidvari, N., Abdelhafez, Y., Wang, Q., Nardo, L., Cherry, S., Badawi, R.: Development of a monte carlo-based scatter correction method for total-body PET using the uEXPLORER PET/CT scanner. *Physics in medicine and biology* **69** (2024) <https://doi.org/10.1088/1361-6560/ad2230>
- [20] Jahangir, R., Kamali-Asl, A., Arabi, H., Zaidi, H.: Strategies for deep learning-based attenuation and scatter correction of brain 18F-FDG PET images in the image domain. *Medical Physics* **51**(2), 870–880 (2024) <https://doi.org/10.1002>

- [21] Guo, R., Xue, S., Hu, J., Sari, H., Mingels, C., Zeimpekis, K., Prenosil, G., Wang, Y., Zhang, Y., Viscione, M., Sznitman, R., Rominger, A., Li, B., Shi, K.: Using domain knowledge for robust and generalizable deep learning-based CT-free pet attenuation and scatter correction. *Nature Communications* **13**, 5882 (2022) <https://doi.org/10.1038/s41467-022-33562-9>
- [22] Laurent, B., Bousse, A., Merlin, T., Nekolla, S., Visvikis, D.: PET scatter estimation using deep learning U-Net architecture. *Physics in Medicine & Biology* **68**(6), 065004 (2023) <https://doi.org/10.1088/1361-6560/ac9a97>
- [23] Shepp, L.A., Vardi, Y.: Maximum likelihood reconstruction for emission tomography. *IEEE Transactions on Medical Imaging* **1**(2), 113–122 (1982)
- [24] Hudson, H.M., Larkin, R.S.: Accelerated image reconstruction using ordered subsets of projection data. *IEEE Transactions on Medical Imaging* **13**(4), 601–609 (1994)
- [25] Knoll, G.F.: *Radiation Detection and Measurement*. John Wiley & Sons, ??? (2010)
- [26] Ronneberger, O., Fischer, P., Brox, T.: U-net: Convolutional networks for biomedical image segmentation. *CoRR* **abs/1505.04597** (2015) [arXiv:1505.04597](https://arxiv.org/abs/1505.04597)
- [27] Chollet, F., et al.: Keras. Accessed: 2022-06-06 (2015). <https://keras.io>
- [28] Abadi, M., Agarwal, A., Barham, P., Brevdo, E., Chen, Z., Citro, C., Corrado, G.s., Davis, A., Dean, J., Devin, M., Ghemawat, S., Goodfellow, I., Harp, A., Irving, G., Isard, M., Jia, Y., Kaiser, L., Kudlur, M., Levenberg, J., Zheng, X.: *TensorFlow : Large-Scale Machine Learning on Heterogeneous Distributed Systems* (2015)
- [29] Kingma, D., Ba, J.: Adam: A method for stochastic optimization. *International Conference on Learning Representations* (2014)
- [30] Segars, W.P., Sturgeon, G., Mendonca, S., Grimes, J., Tsui, B.M.W.: 4d XCAT phantom for multimodality imaging research: 4D XCAT phantom for multimodality imaging research. *Medical Physics* **37**(9), 4902–4915 (2010) <https://doi.org/10.1118/1.3480985>
- [31] Ferrero, A., Poon, J.K., Chaudhari, A.J., MacDonald, L.R., Badawi, R.D.: Effect of object size on scatter fraction estimation methods for PET—A computer simulation study. *IEEE Transactions on Nuclear Science* **58**(1), 82–86 (2011) <https://doi.org/10.1109/TNS.2010.2080685>
- [32] Le Maitre, A., Segars, W.P., Marache, S., Reilhac, A., Hatt, M., Tomei, S., Lartizien, C., Visvikis, D.: Incorporating patient-specific variability in the simulation of realistic whole-body  $^{18}\text{F}$ -fdg distributions for oncology applications. *Proceedings of the IEEE* **97**(12), 2026–2038 (2009) <https://doi.org/10.1109/JPROC.2009.2027925>
- [33] Peña-Acosta, M.M., Gallardo, S., Lorduy-Alós, M., Verdú, G.: Application of nema protocols to verify gate models based on the digital biograph vision and the biograph vision quadra scanners. *Zeitschrift für Medizinische Physik* (2024) <https://doi.org/10.1016/j.zemedi.2024.01.005>
- [34] Salvadori, J., Merlet, A., Presles, B., Cabello, J., Su, K.-H., Cochet, A., Etxebeste, A., Vrigneaud, J.-M., Sarrut, D.: Pet digitization chain for monte carlo simulation in gate. *Physics in Medicine & Biology* **69**(16), 165013 (2024) <https://doi.org/10.1088/1361-6560/ad638c>
- [35] Jan, S., Santin, G., Strul, D., Staelens, S., Assié, K., Autret, D., Avner, S., Barbier, R., Bardiès, M., Bloomfield, P.M., Brasse, D., Breton, V., Bruyndonckx, P., Buvat, I., Chatziioannou, A.F., Choi, Y., Chung, Y.H., Comtat, C., Donnarieix, D., Ferrer, L., Glick, S.J., Groiselle, C.J., Guez, D., Honore, P.-F., Kerhoas-Cavata, S., Kirov, A.S., Kohli, V., Koole, M., Krieguer, M., Laan, D.J., Lamare, F., Largeron, G., Lartizien, C., Lazaro, D., Maas, M.C., Maigne, L., Mayet, F., Melot, F., Merheb, C., Pennacchio, E., Perez, J., Pietrzyk, U., Rannou, F.R., Rey, M., Schaart, D.R., Schmidlein, C.R., Simon, L., Song, T.Y., Vieira, J.-M., Visvikis, D., Walle, R.V., Wieërs, E., Morel, C.: GATE: a simulation toolkit for PET and SPECT. *Physics in Medicine and Biology* **49**(19), 4543–4561 (2004) <https://doi.org/10.1088/0031-9155/49/19/4543>

- [36] Ghabrial, A., Franklin, D., Zaidi, H.: A monte carlo simulation study of scatter fraction and the impact of patient BMI on scatter in long axial field-of-view PET scanners. *Zeitschrift für Medizinische Physik* **31** (2021) <https://doi.org/10.1016/j.zemedi.2021.01.006>
  
- [37] Hatt, M., Rest, C., Turzo, A., Roux, C., Visvikis, D.: A fuzzy locally adaptive bayesian segmentation approach for volume determination in PET. *IEEE Transactions on Medical Imaging* **28**(6), 881–893 (2009) <https://doi.org/10.1109/TMI.2008.2012036>